SUNSPOT ROTATION AS A DRIVER OF MAJOR SOLAR ERUPTIONS IN THE NOAA ACTIVE REGION 12158

P. Vemareddy[1], X. Cheng[2], AND B. Ravindra[1]
[1] Indian Institute of Astrophysics, Koramangala, Bangalore-560034, India; vemareddy@iiap.res.in
[2] School of Astronomy and Space Science, Nanjing University, Nanjing-210023, China

ABSTRACT

We studied the development conditions of sigmoid structure under the influence of the magnetic non-potential characteristics of a rotating sunspot in the active region (AR) 12158. Vector magnetic field measurements from the Helioseismic Magnetic Imager and coronal EUV observations from the Atmospheric Imaging Assembly reveal that the erupting inverse-S sigmoid had roots at the location of the rotating sunspot. The sunspot rotates at a rate of $0°$–$5° \, h^{-1}$ with increasing trend in the first half followed by a decrease. The time evolution of many non-potential parameters had a good correspondence with the sunspot rotation. The evolution of the AR magnetic structure is approximated by a time series of force-free equilibria. The non-linear force-free field magnetic structure around the sunspot manifests the observed sigmoid structure. Field lines from the sunspot periphery constitute the body of the sigmoid and those from the interior overlie the sigmoid, similar to a flux rope structure. While the sunspot was rotating, two major coronal mass ejection eruptions occurred in the AR. During the first (second) event, the coronal current concentrations were enhanced (degraded), consistent with the photospheric net vertical current; however, magnetic energy was released during both cases. The analysis results suggest that the magnetic connections of the sigmoid are driven by the slow motion of sunspot rotation, which transforms to a highly twisted flux rope structure in a dynamical scenario. Exceeding the critical twist in the flux rope probably leads to the loss of equilibrium, thus triggering the onset of the two eruptions.

Key words: Sun: corona – Sun: coronal mass ejections (CMEs) – Sun: evolution – Sun: flares – Sun: magnetic fields – Sun: photosphere

1. INTRODUCTION

It is generally believed that major solar eruptions, including flares and coronal mass ejections (CMEs), are powered by the free energy stored in the stressed magnetic fields in the so-called active regions (ARs). These stressed fields transport magnetic energy and helicity during the evolution of ARs primarily by the mechanisms of flux emergence from the sub-photosphere and the foot point shearing motions at the photosphere. Of the many important features, sunspot rotations are a form of uncommonly observed motions, lasting even for days, during the evolution of the ARs (Evershed 1910; Bhatnagar 1967; McIntosh 1981, pp. 7–54; Brown et al. 2003; Zhang et al. 2007), and are suggested to be efficient mechanisms for injecting helicity and energy (e.g., Stenflo 1969; Barnes & Sturrock 1972; Amari et al. 1996; Tokman & Bellan 2002; Török & Kliem 2003).

With the increase of observational capabilities both in sensitivity and resolution, sunspot rotation has drawn considerable attention in an attempt to explain its characteristics in association with transient activity. A majority of the studies based on observations have examined the relationship between sunspot rotation and the coronal consequences (Brown et al. 2003; Tian & Alexander 2006; Tian et al. 2008), flare productivity (Yan et al. 2008; Zhang et al. 2008; Suryanarayana 2010), the association of flares with abnormal rotation rates (Hiremath & Suryanarayana 2003; Jiang et al. 2012b), non-potential parameters (Zhang et al. 2007; Kazachenko et al. 2009; Vemareddy et al. 2012a), and helicity injection (Vemareddy et al. 2012b) etc.

Numerical magnetohydrodynamic (MHD) investigations have also helped greatly in understanding the relationship between sunspot rotation and eruptive activity by studying the formation and evolution of flux ropes by twisting line-tied

potential fields (Mikic et al. 1990; Amari et al. 1996; Galsgaard & Nordlund 1997; Gerrard et al. 2002). The underlying idea of these simulations is to show that the photospheric vortex motions can twist the core magnetic field in an AR up to a point where equilibrium can no longer be maintained and thus the twisted core field i.e., flux rope, erupts (Tokman & Bellan 2002; Török & Kliem 2003; Amari et al. 2010; Aulanier et al. 2010). At the instant of exceeding the critical twist, the flux rope is subjected to helical kink instability (Török & Kliem 2005). Depending on the decay rate of the restoring force by the overlying field, the progressive injection of the twist in the underlying flux rope is shown to erupt as a confined flare or a CME. As a secondary possibility, twisting motions could also weaken the stabilizing overlying field of the flux rope. A recent numerical model by Török et al. (2013) demonstrates the rotating sunspot as a trigger by inflating the field passing over a pre-existing flux rope, resulting in a weakening of the downward tension force of the overlying field. In retrospect, however, the twisting motions can twist both the overlying field and the flux rope, because there is no pure current-free field to stabilize the entire flux rope system. Recent observational analysis (e.g., Vemareddy & Zhang 2014) indicates that the kink instability could be the onset of eruption, bringing the flux rope to the height of the inflating field, from where the eruption is further driven by torus instability.

Although the above proof-of-concept simulations strikingly explain and reproduce the many observed features of eruptions, not many observational studies exist to reconcile the development/formation scenario of the flux rope in the host AR of the rotating sunspot. In the present paper, we study the development conditions of sigmoid structure under the influence of the non-potential characteristics of a rotating sunspot in an AR. Using uninterrupted, high-cadence magnetic field observations

of AR 11158 at the photosphere, Vemareddy et al. (2012a) reported an unambiguous correspondence of sunspot rotation with many non-potential parameters including energy and helicity deposition rates. In that AR, occurrence of the major flares and CMEs are shown to be co-temporal with the peak rotation rates of sunspots (Jiang et al. 2012b; Vemareddy et al. 2015). Importantly, the observed characteristics of those non-potential parameters could have their origins in sub-photospheric twist because the AR 11158 was emerging. So for the cause–effect relation, it would be of great interest to investigate a case of sunspot rotation in the post-phase of AR emergence, which is the subject of this paper. Motivated by these studies, we model the AR magnetic structure by nonlinear force-free approximations and examine the coronal field topology and current distribution in favor of the flux rope. Observations are outlined in Section 2; results, including measurement of sunspot rotation, non-potential characteristics, and force-free extrapolation, are described in Section 3. A summary of the results with a discussion is presented in Section 4.

2. OBSERVATIONS

The major source of observational data for our study is from the *Solar Dynamic Observatory*. The Heliosesmic Magnetic Imager (HMI; Schou et al. 2012) captures full-disc line-of-sight magnetic field measurements at a cadence of 45 s and vector magnetic fields at a cadence of 135 s. For the sunspot rotation study, we use continuum intensity observations at 45 s cadence. In order to quantify non-potentiality due to the effect of sunspot rotation on the magnetic field, we obtained vector magnetic field measurements at a cadence of 12 minutes provided after pipelined procedures of inversion and disambiguation (Bobra et al. 2014; Hoeksema et al. 2014). The corresponding coronal activity is studied by multi-thermal EUV images taken by the Atmospheric Imaging Assembly (AIA; Lemen et al. 2012) at a cadence of 12 s.

3. RESULTS

The AR of interest was NOAA 12158, which appeared on the solar disk during 2014 September 5–14. It was located on the northern hemisphere at $15°$ latitude. It is a pre-emerged AR with an approximately bipolar magnetic field configuration. During its disk passage, the complexity of the magnetic configuration ranges from simple α to $\alpha\beta\gamma$. Apart from small-scale activity, two major CME eruptions occurred, which are associated with M and X class flares from this AR. The coronal observations captured in multi-wavelengths show a large-scale sigmoidal structure. One of its legs has roots from a major sunspot of positive polarity. During the time interval of 2014 September 7–11, the composite images prepared from multi-layered observations presented multi-thermal plasma loops. During a few sigmoid eruptions, these images clearly identified the presence of a hot sigmoid channel surrounded by cool plasma loops (Figure 1, first column panels). This sigmoid is regarded as a magnetic flux rope (Zhang et al. 2012; Cheng et al. 2013; Vemareddy & Zhang 2014) to connect with the theories of flux-rope-based models to explain CME eruptions.

Vector magnetic fields observed by the HMI show a main sunspot of positive polarity surrounded by plage-type distributed negative polarity. The overall chirality of the transverse vectors aligns in a left-handed sense. This sense of

chirality explains the coronal geometry of magnetic loops which manifests a reverse S-sigmoid (middle column panels of Figure 1). Interestingly, the motion images of these vector magnetograms reveal rotation of this main sunspot as anti-clockwise while the AR evolves persists with this global sigmoidal structure. To identify the photospheric magnetic connections of the coronal plasma structures, we overlaid contours of magnetic concentrations. They unambiguously show that the sigmoid has roots in that sunspot, indicating that the sunspot rotation has a direct role in progressively building this sigmoidal structure. We used these magnetic field observations to follow the flux motions due to the sunspot rotation. By employing the differential affine velocity estimator for vector magnetograms (DAVE4VM; Schuck 2008), we derived the velocity field of the flux motions. In Figure 1 (last column panels), the horizontal velocity field is overlaid on the HMI continuum intensity maps. The orientation of these velocity vectors conspicuously indicates the swirling motion of fluxes owing to sunspot rotation in an anti-clockwise direction. In particular, the fluxes from the western part of the penumbral region exhibits more of this apparent rotation.

3.1. Measurement of Sunspot Rotation

Qualitative measurements of the rotating sunspots are made by preparing the stack plots of a radial section in the penumbra (Brown et al. 2003; Zhang et al. 2008; Vemareddy et al. 2012a). The idea essentially is to track the motion of any penumbral feature in time while the sunspot rotates about its umbral center (Figure 2(a)). For this, the penumbral region is unstretched (anti-clockwise direction from the west) by remapping onto the radius-theta plane. We used continuum intensity images from the HMI at a cadence of 12 minutes. A snapshot of such an unstretched penumbra in Figure 2(a) of our sunspot of interest is shown in Figure 2(b). The stack plots (spacetime) are then made by assembling slits taken at a radial position sequentially in time. In panels (c) and (d) of Figure 2, the stack plots prepared from two different radial positions (5 and 10 pixels from umbra and penumbra boundary) are shown. Since this sunspot rotates in an anti-clock direction, we can see the feature motion with increasing angle. The inclination, in time, of penumbral fibrils also delineates a similar physical motion. From these stack plots, we have followed the prominently observed feature (dashed yellow curves) motion to derive information about the rate of rotation. Note that the feature resembling a white curve is an artifact due to missing data in a row (namely, Figure 1 (last column)) of the intensity image frames.

From the curves, different features have varying rotation rates in time. Most of the features disappear (or fall into umbra) in a short period of time. Hence it is difficult to track the rotation uniquely with the same feature. On September 7, the feature motion is steep followed by a slowing down on September 8. In the first quarter of September 9, the features stagnate in time. This suggests the slow-down of sunspot rotation, as also found in the case of AR 11158 (Vemareddy et al. 2012a, 2015). The magnetic tension in the field lines connecting the sunspot and the opposite negative polarity is suggested to play a predominant role in the slow-down of the sunspot rotation. As the sunspot rotates slowly, the magnetic stress in the field lines from the sunspot increases. After a critical point, the tension in these field lines opposes any further rotation. This critical state can also be regarded as non-potential
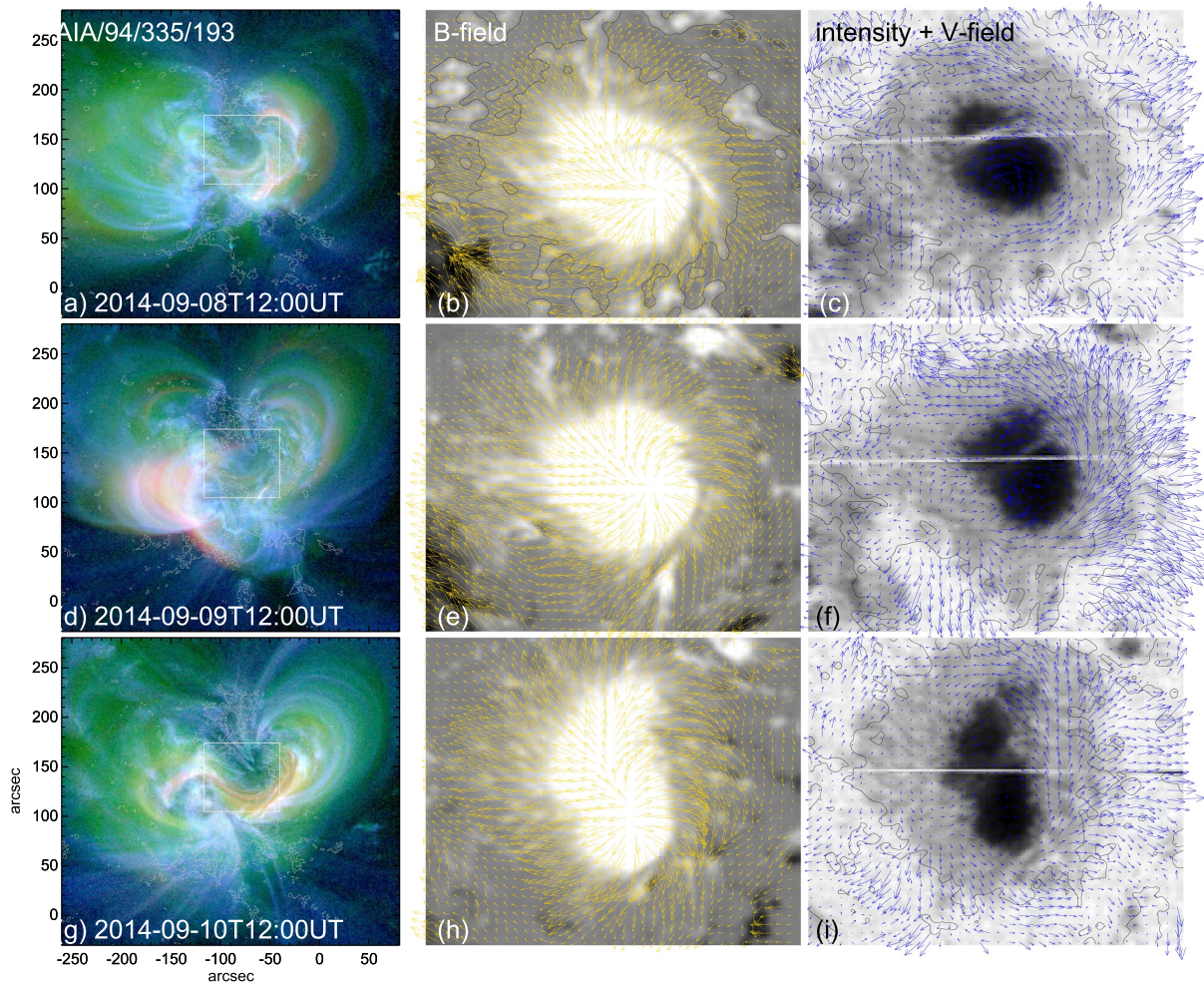
Figure 1. Association of sigmoid structure with the sunspot rotation in AR 12158. First column: snapshots of the corona sigmoid in composite temperatures prepared from AIA 94, 335, 193 Å channels. The rectangular region indicates the region of rotating sunspot having roots of the sigmoid. Contours of B_z (±150 G) are overlaid to identify the photospheric connections of the sigmoid. Second column: vector magnetograms of the rectangular region, showing the magnetic field in the rotating sunspot. The background is the vertical field component and arrows show the direction and magnitude of the horizontal field. Third column: horizontal velocity field overplotted on the HMI continuum intensity map of the rotating sunspot. Note the anti-clockwise orientated velocity vectors on the west portion due to the sunspot rotation.

due to the stored energy. At this point, any kind of instability may trigger the release of energy. Not surprisingly, a CME eruption is launched at 23:00UT on September 8, followed by an M4.6 flare at 23:12UT. In AR11158 also, at the time (18:00UT on 2011 February 14) of slow-down of the sunspot rotation, a major CME eruption is triggered followed by an M2.2 flare. This is a direct consequence of the often observed sunspot rotation harboring powerful CMEs. The cause of sunspot rotation is likely related to sub-photospheric dynamics, which cannot be probed by photospheric observations.

Once the tension in the connected field lines is released by an eruption, the sunspot rotation may continue depending on the driving force beneath the photosphere. Here in our case, after the first eruption, the sunspot rotates until September 11. The feature motion is ambiguous as to whether we can infer any further cessation of rotation; however another powerful eruption launched at 17:15UT on September 10, followed by an X1.6 flare at 17:21UT. From these observational cases, we suggest that the slow-down of the sunspot rotation is an indicator of the triggering of major powerful eruptions.

From the time profiles of the rotation, we derived rotation rates ($d\theta/dt$) of the different features. We found them to rotate at varying rates. A feature that exists for a long time has $d\theta/dt$ of $0°$–$4°\ h^{-1}$. However, there are short-lived features (6–8 hr, in $0°$–$100°$ section) that rotate rapidly, even up to $8°\ h^{-1}$. In all, sunspot rotation is neither uniform spatially nor constant over time.

3.2. Evolution of Magnetic Non-potential Parameters

In the presence of the unusual rotating sunspot in the AR, it is imperative to study the evolution of magnetic non-potentiality. This is quantified by many parameters, but a few of them that can be estimated with the photospheric vector magnetograms ($\boldsymbol{B}$) are net vertical current, α_{av}, helicity injection, and Poynting flux etc. The vertical current distribution is calculated using

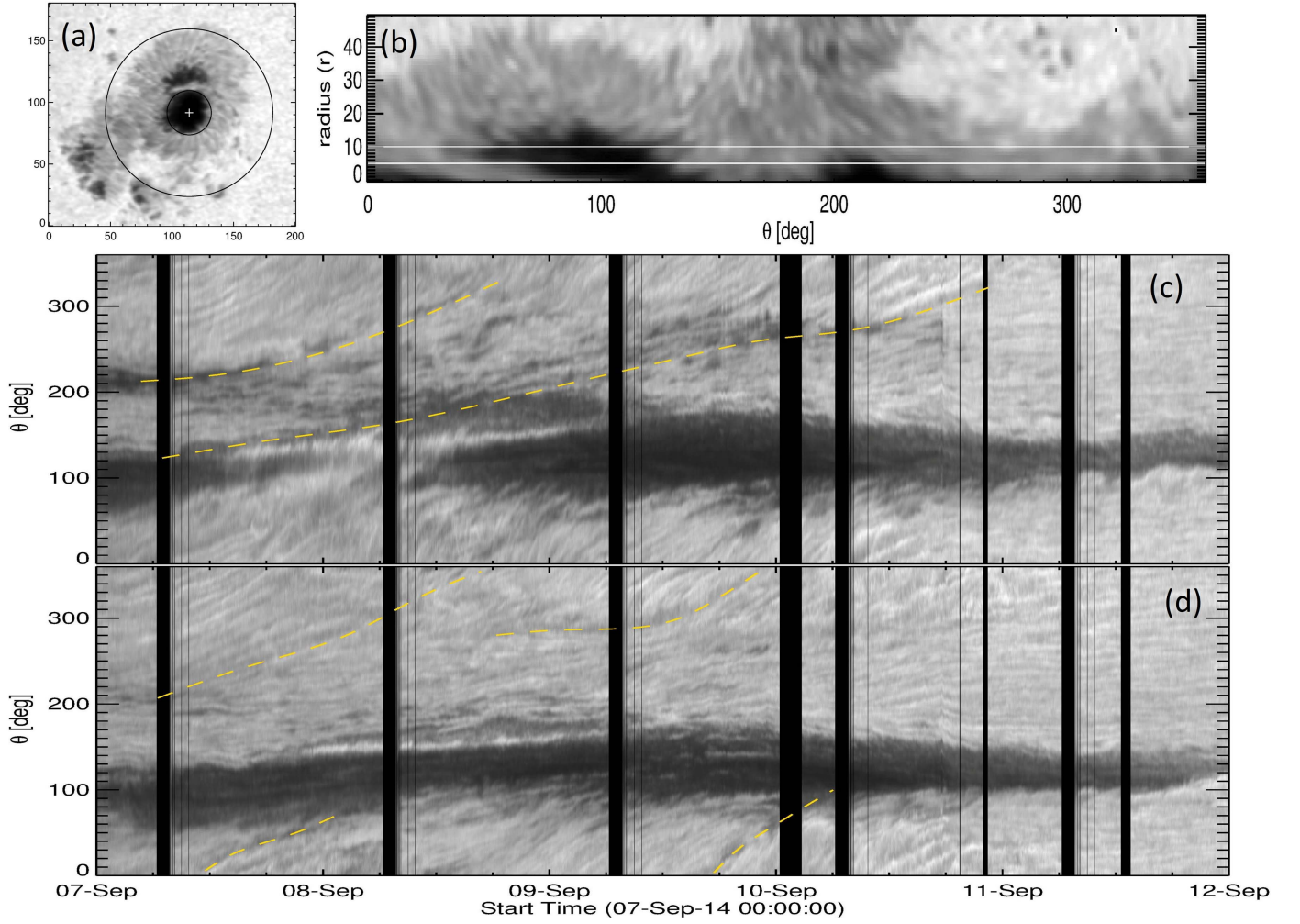$$j_z = \frac{(\nabla \times \boldsymbol{B})}{\mu_0}, \tag{1}$$

Figure 2. Measurement of the sunspot rotation (a) Snapshot of the sunspot showing the located centroid ("+") and penumbral region between two concentric circles, (b) r–θ map prepared after unstretching the annular region of penumbra of the sunspot. Two horizontal lines indicate the radial positions of the slits to prepare the stack plot of slices, (c) and (d) space–time (stack plots) maps at two radial positions from the umbral center. The angular movement of different features refers to the sunspot anti-clockwise rotation. Dashed curves represent the angular motion of some prominent features. Also note that the sunspot features encounter slow-down/stop during the first half of September 9. Vertical black strips correspond to data gaps and turquoise lines indicate the times of the two eruptions.

where $\mu_0 = 4\pi \times 10^{-7}$ Henry m^{-1}. The extent of averaged twistedness of the magnetic structure in the AR is estimated by

$$\alpha_{av} = \frac{\sum J_z(x, y) \mathrm{sign}[B_z(x, y)]}{\sum |B_z|} \quad (2)$$

(Hagino & Sakurai 2004). The sign of this parameter generally gives the handedness or chirality of the magnetic field. The helicity injection rate relates the flux motions with the observed twisted magnetic field (Berger & Field 1984) by

$$\frac{dH}{dt}\bigg|_S = 2\int_S (\boldsymbol{A}_P \cdot \boldsymbol{B}_t)\mathrm{V}_{\perp n} dS - 2\int_S (\boldsymbol{A}_P \cdot \boldsymbol{V}_{\perp t})\mathrm{B}_n dS \quad (3)$$

where $\boldsymbol{A}_p$ is the vector potential of the potential field $\boldsymbol{B}_p$, $\boldsymbol{B}_t$ and B_n denote the tangential and normal magnetic fields, and $\boldsymbol{V}_{\perp t}$ and $\boldsymbol{V}_{\perp n}$ are the tangential and normal components of velocity $\boldsymbol{V}_\perp$, the velocity perpendicular to the magnetic field lines. The velocity field ($\boldsymbol{V}$) is derived from time sequence vector magnetic field observations obtained from the HMI by employing the DAVE4VM technique. Similarly, the magnetic energy (Poynting) flux across the surface (Kusano et al. 2002),

can be estimated as

$$\frac{dE}{dt}\bigg|_S = \frac{1}{4\pi}\int_S B_t^2 V_{\perp n} dS - \frac{1}{4\pi}\int_S (\boldsymbol{B}_t \cdot \boldsymbol{V}_{\perp t})B_n dS \quad (4)$$

Procedures involving the estimation of these parameters are widely described in many recent studies (e.g., Liu & Schuck 2012; Vemareddy et al. 2012a, 2012b; Vemareddy 2015) in different contexts. Following similar procedures, we calculated these parameters in this AR and plot their time evolution in Figure 3. The net flux from north and south polarity shows a monotonic decrease from the start of the observation interval. The imbalance of the flux content in the AR is in the range of 7%–11%. The net vertical current in the north (I_N) polarity is negative and varies from -3×10^{12} A to -6.5×10^{12}A. On the other hand, it is positive in the south polarity (I_S), varying from 3×10^{12} A to 6×10^{12} A. As the sunspot continues to rotate, the shear in the horizontal vectors increases, which in turn contributes to the net vertical currents in the form of horizontal field gradients, as both of these currents have reached their maximum values by the
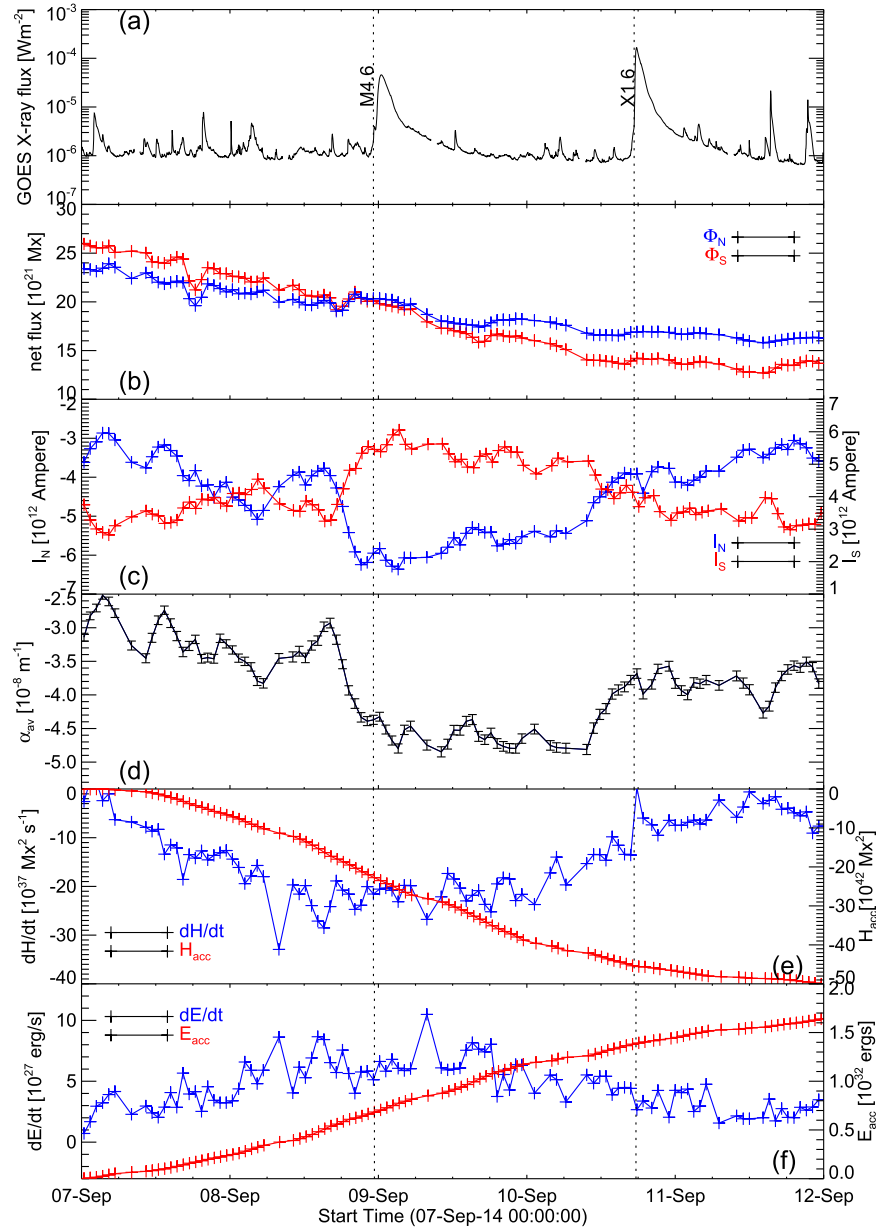
Figure 3. Evolution of different magnetic parameters in the AR 12158 (a) GOES X-ray flux, indicating the onset M4.6 and X1.6 flares associated with CME eruptions, (b) decreasing net flux in both polarities, (c) net vertical current integrated from each polarity, (d) linear force-free average α with first increasing and then decreasing trend, (e) helicity injection rate, (f) Poynting flux. The overall trend of α_{av} correlates with that of the time rate of helicity injection. The dominant net negative (positive) vertical current in the north (south) polarity signifies the negative or left-handed nature of the AR magnetic structure, consistent also with the helicity injection rate. Dotted vertical lines refer to timings of flares associated with the two eruptions.

time of cessation of the sunspot rotation. As per these current profiles, α_{av} also shows an initial increasing trend up to $-4.7 \times 10^{-8}\,\mathrm{m}^{-1}$ until the time of the first eruption and then decreases, followed by a major eruption at 17:30UT on September 10.

The time profile of dH/dt also exhibits a similar trend as the net current and α_{av}. The order of the estimated values of dH/dt and ΔH are consistent with earlier studies (e.g., Vemareddy et al. 2012a, 2012b). It is worth pointing out that the dominant net negative (positive) vertical current in the north (south) polarity signifies the negative or left-handed nature of the AR magnetic structure, consistent also with the helicity injection rate. All these profiles suggest that the non-potentiality is a direct consequence

of organized flux motions generated by the sunspot rotation. Energy flux injection is positive and is on the order of $10^{27}\,\mathrm{erg\,s}^{-1}$. The accumulated energy over the time interval before the occurrence of the eruption and the associated flare is of the order of $32\,\mathrm{erg}$, which is suffice to generate a flare of magnitude up to GOES class X. A similar observational result follows from the study of the sunspot rotation in AR 11158 (Vemareddy et al. 2012a, 2012b), where the peak phase (in magnitude) of different non-potential parameters coincides with the occurrence of the major eruptions and associated flares. This demonstrates that the successive accumulation of non-potentiality is mainly due to the surface motion (shear/twist) on the photosphere but not the flux emergence.
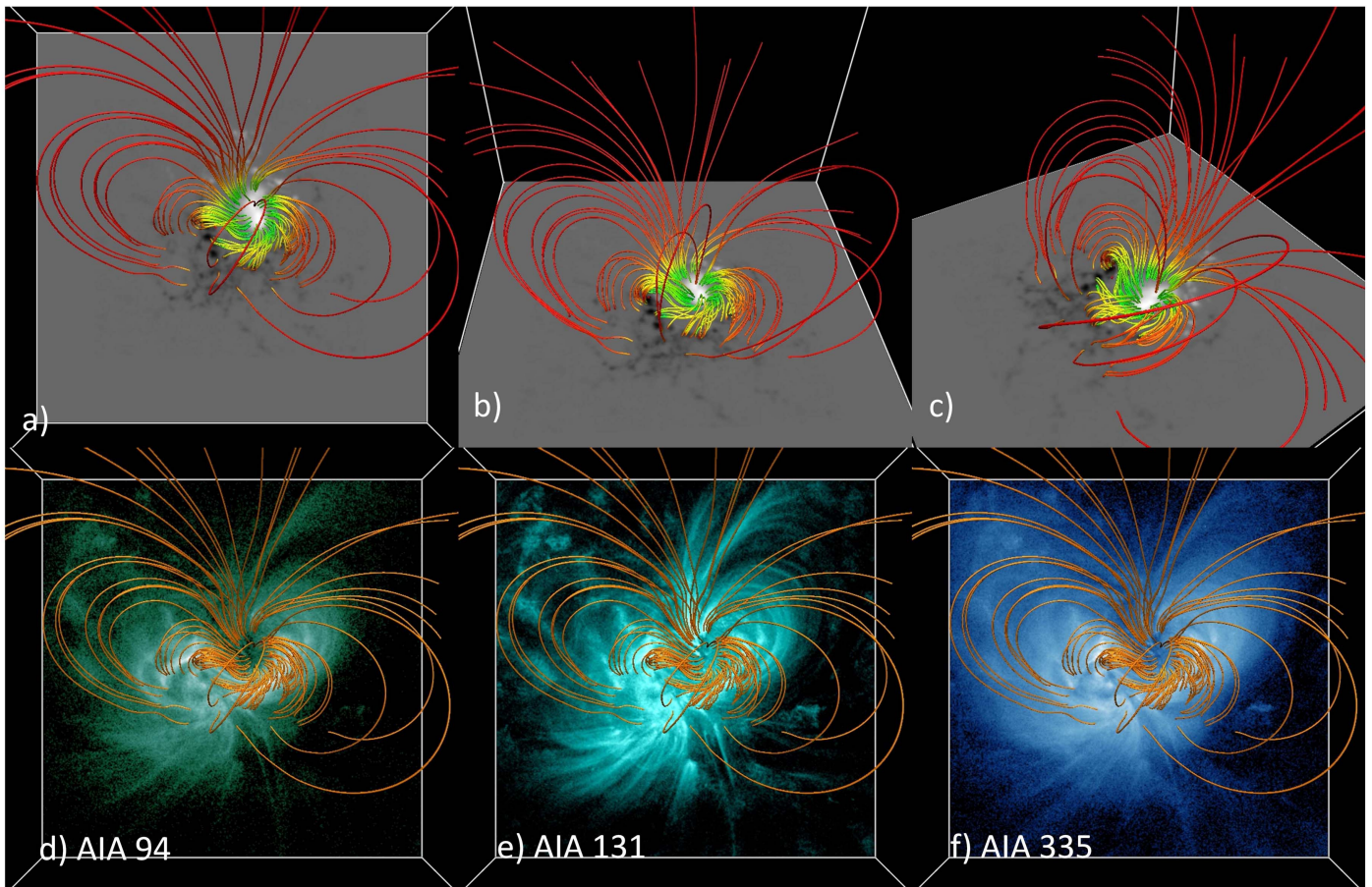
Figure 4. Magnetic structure in AR 12158 at 12:00UT on 2014 September 10. (a)–(c) Traced field lines imaged over B_z. Field lines from the periphery of the sunspot manifest the body of the sigmoid and those from the interior overlie the sigmoid. (d)–(f) Field structure on the AIA images reflecting the resemblance of a flux rope structure.

3.3. Non-linear Force-free Modeling

In order to realize the effect of sunspot rotation on the geometry of the AR magnetic structure, we performed nonlinear force-free field (NLFFF) extrapolation (Wiegelmann 2004; Wiegelmann & Inhester 2010) of the observed photospheric magnetic field. The field of view of the boundary field covers the full AR such that flux is nearly balanced over the entire time interval. To satisfy the force-free conditions, the magnetic components are subject to a pre-processing procedure (Wiegelmann et al. 2006). To facilitate tracing field lines in a large extent of volume, the observed boundary is inserted in an extended field of view and computations are performed on a uniformly spaced computational grid of $400 \times 400 \times 256$ representing physical dimensions of $292 \times 292 \times 280 \, \mathrm{Mm}^3$. Before this, we rebinned the observations to 1 arcsec pixel^{-1}. The NLFFF code is initiated with linear force-free field constructed from the normal field component and a small value of the force-free parameter.

With the extrapolated field in the coronal volume above the AR, we traced field lines roughly according to the total current ($|\mathbf{J}|$) and total field strength ($|\mathbf{B}|$). This modeled structure is plotted in Figure 4 with B_z (panels (a)–(c)) and coronal EUV observations (panels (d)–(f)) as the bottom boundary. Field lines from the lower periphery of the sunspot correspond to the middle section (body) of the sigmoid whereas those from the central part serve as the overlying flux system. The right

J-section of the sigmoid is highly curved due to more twisted field lines from the top periphery of the sunspot, where the modeled structure differs significantly. However, the field lines closely resemble the global magnetic structure of the plasma loops of the sigmoid and the surrounding loops, as in earlier modeling studies (Savcheva & van Ballegooijen 2009; Sun et al. 2012). As the sunspot rotates in an anti-clockwise direction, the field lines tend to retain their connectivity, and appear as swirling in the clockwise direction. Due to the high current density, the flux system between the sunspot and its counterpart appears as a hot channel when observed in coronal AIA 131, 94 Å wavelengths.

Now the entire magnetic system is evolving quasi-statically, because the driving boundary motion ($1 \, \mathrm{km \, s^{-1}}$) is far less than the Alfvén timescale of the coronal magnetic field. Therefore, our static modeling cannot capture the features of rapid evolution during sigmoid eruption. However, the gradual build-up, like the flux rope current channel, topologies which are the basic building blocks of eruption models (Török & Kliem 2005; Aulanier et al. 2010), can approximately be captured. A close view of the magnetic structure around the sunspot reveals the effect of sunspot rotation as described in the earlier sections (panel (c)). Due to this twisting motion, especially at the sunspot periphery, the field lines rooted therein had a fan-shaped structure (deviating from radial ones); the field lines rooted near to the center overlie the earlier ones. The two J-sections of the sigmoid are
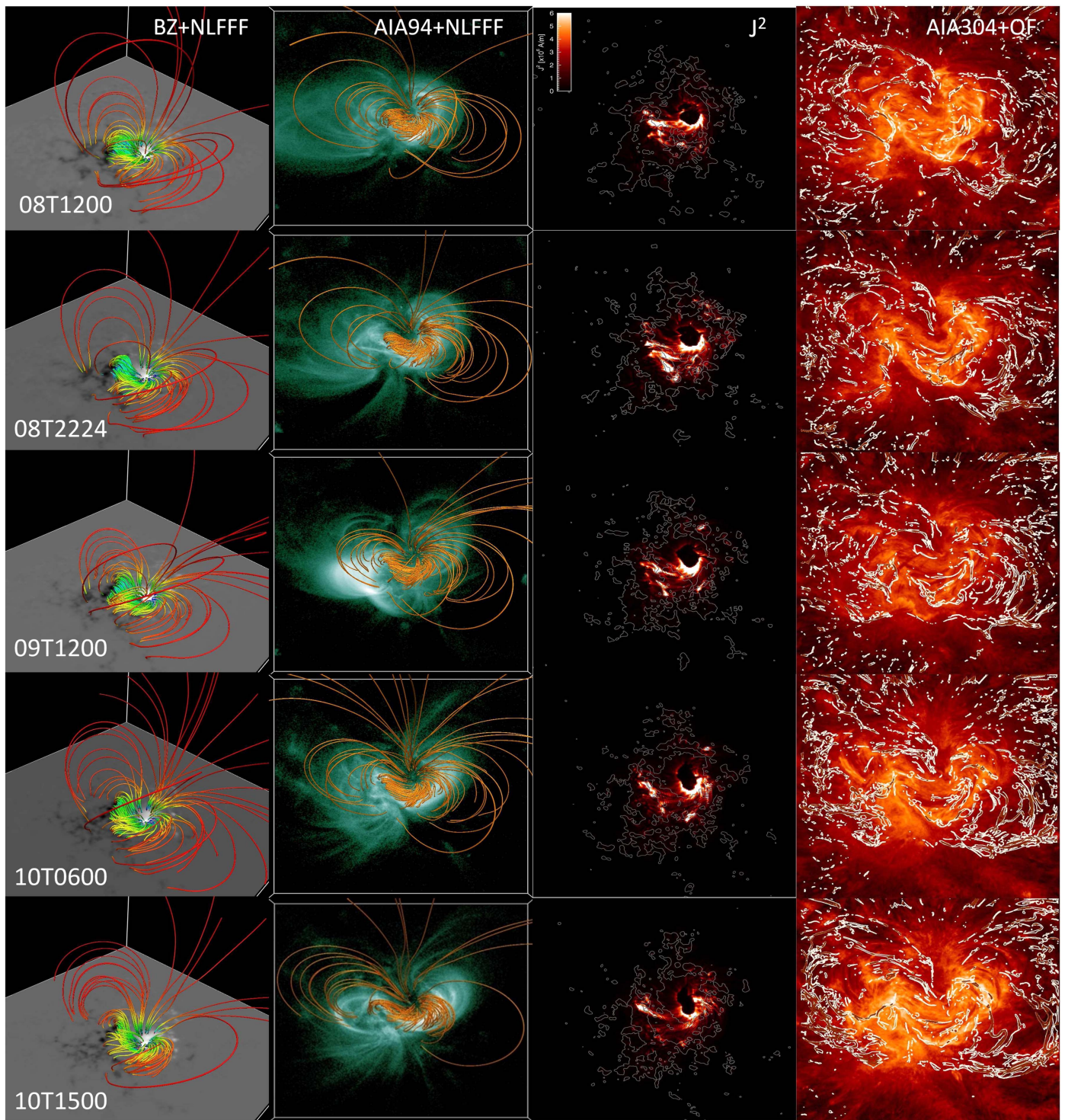
Figure 5. Magnetic structure around the rotating sunspot, from top to bottom, at different epochs. First column: top view of the extrapolated field structure, resembling the sigmoid. Second column: tilted view of the same structure to visualize the stressed nature of the field lines around the sunspot. Third column: vertical integrated maps of current density $|J^2|$ to locate the build-up of strong current concentrations. Fourth column: AIA 304 Å images overlaid by contours of the quashing factor. EUV emission along the sigmoid outlines the higher QF values and indicates co-spatial location of the highly stressed magnetic field and current concentration.

compact and curved, which the NLFFF code fails to reproduce exactly.

For a view of quasi-static evolution, in Figure 5 (columns 1 and 2), we plot the magnetic structure in the sigmoid at different epochs of the sunspot rotation. To capture the sheared field lines around the sunspot, field lines are rendered according to higher current density criteria. Highly sheared field lines originate from

the lower periphery of the sunspot and they lie mostly below 10 Mm in height. The two J-sections of the sigmoid are compact and curved, which the NLFFF code fails to reproduce exactly. In such a flux system being slowly driven by constant rotational motion, the formation of the flux rope in the dynamic scenario is inevitable. Moreover, it appears that continuous sunspot rotation helps sustain the flux rope structure throughout the evolution.
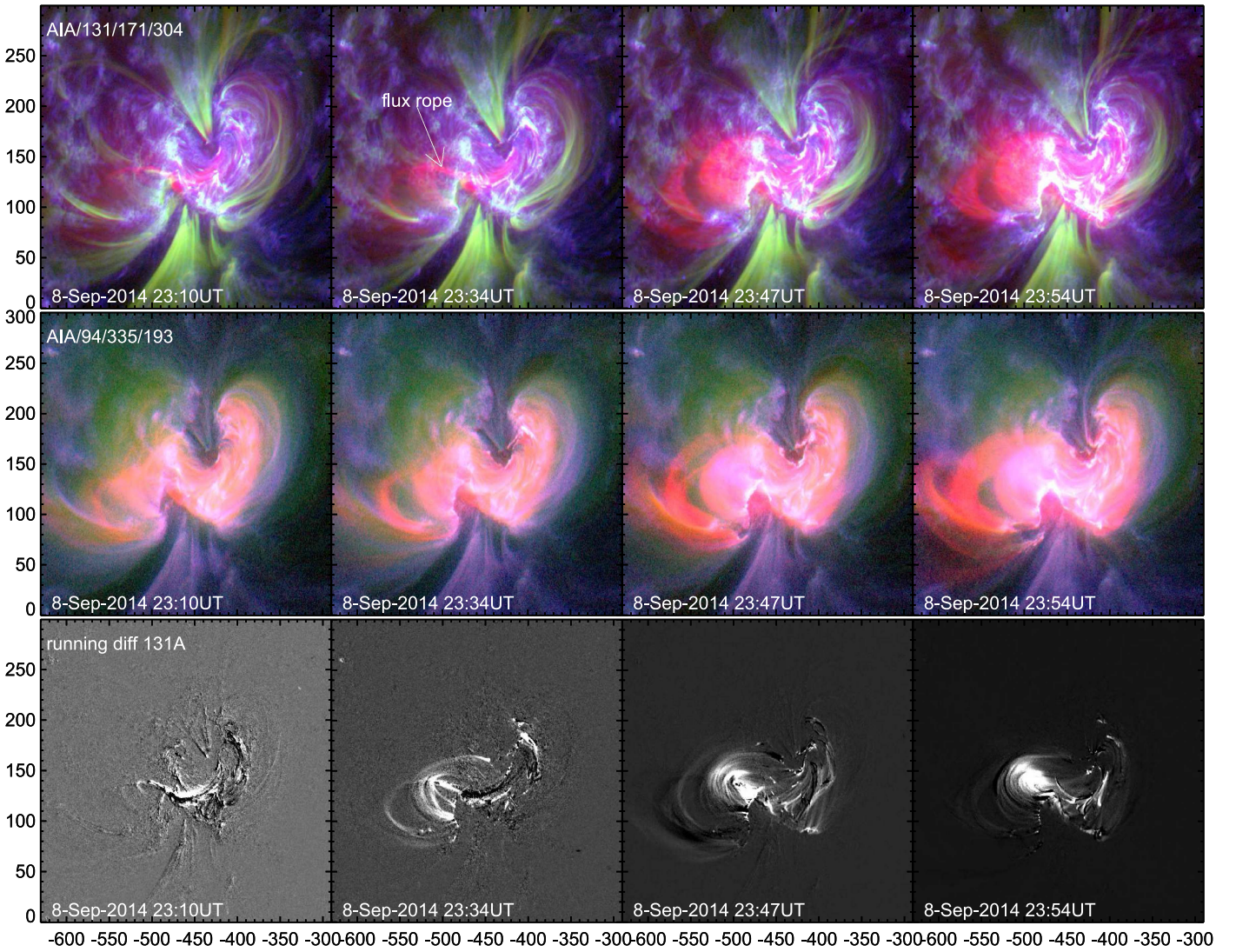
Figure 6. Onset scenario of sigmoid eruption on 2014 September 8 at around 23:55UT. Top row: composite images of the corona observed at different temperatures of the AIA 131, 171 and 304 Å channels. Note the flux rope as a hot continuous trace during its onset of slow rise motion. Middle row: composite images of the corona in another combination of AIA temperature channels (AIA/94/335/193). Note the enhancing hot flux bundle (flux rope) in the middle of the sigmoid structure. Bottom row: running difference images of the AIA 131 Å showing the rising sigmoidal structure before the onset of the CME. The timing of this eruption precedes the drastic increase of net vertical current and α_{av}. All panels are in heliographic arcsec units.

The current density characterizes the non-potentiality of the field. The patterns of strong current concentration serve as a proxy to the non-potential structure in the corona. Moreover, current structures are regions where reconnection can occur to convert magnetic energy to thermal and kinetic energy. Dense distribution of current persists mostly around the lower portion of the sunspot up to a height of 10 Mm. This immense coronal current distribution is due to an increasingly developing sheared arcade interfacing the rotating sunspot and the surrounding negative polarity at the lower half portion. We compute the vertical integration of J^2 (i.e., $\int_z J^2 dz$) (column 3 in Figure 5). As the J^2 term is proportional to the Joule heating term, it thus roughly represents the hot emission. This is indeed true in our case. The strong current concentration around the sunspot spatially coincides with the high intensity of EUV emission in the 304 Å images, especially the south circular portion due to the highly stressed magnetic field.

To measure the magnetic field line linkage, we also compute the quashing factor (QF) (Titov et al. 2002). Higher values of the QF locate the quasi-separatrix layers which are the sources of high current concentration. The contours of the QF on AIA 304 Å observations are shown in Figure 5 (fourth column panels). The traces of high QF values roughly outline the sigmoid in all the time shots. The difficulty of reproducing curved, compact J-sections is well acknowledged due to the insufficient observational sensitivity of the HMI (Nindos et al. 2012; Sun et al. 2012; Vemareddy & Wiegelmann 2014). Owing to this difficulty, reproducing a flux rope structure with the extrapolation technique is deemed to be a challenge and different treatments to the boundary observations (e.g., Jiang et al. 2012a, 2014; Zhao et al. 2016) are being employed in different extrapolation codes. The optimization code relies on observed horizontal field components and globally relaxes toward force-free equilibrium. Without any treatment, the model remarkably shows many similarities of the flux rope structure around the rotating sunspot. In the following, we explore the evolution of the magnetic structure around the sunspot over the time of the two observed major eruptions.
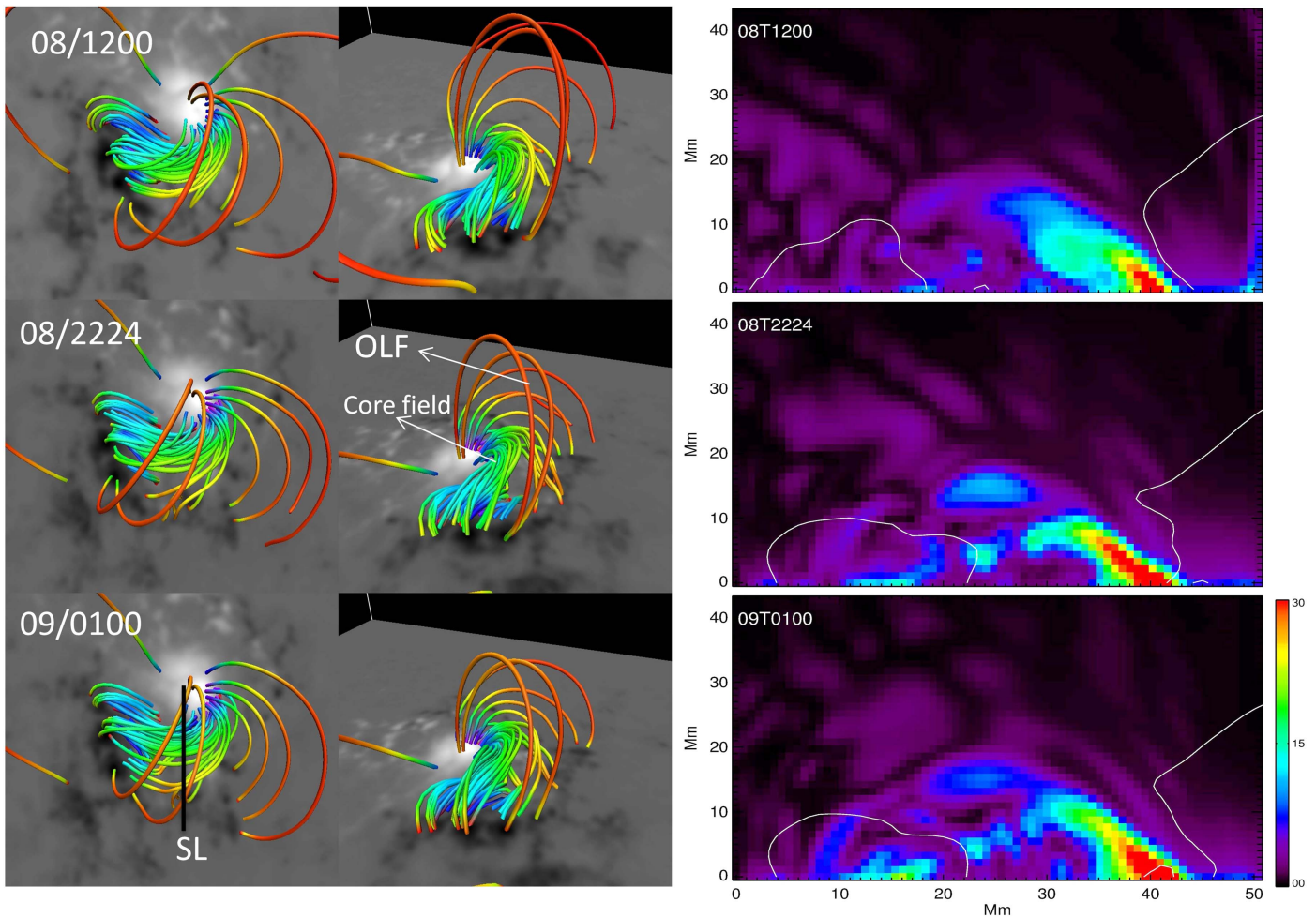
Figure 7. Scenario of flux rope development from the sheared arcade around the sigmoid eruption event of September 8, at 23:55UT. First column: top view of the field structure rendered from the rotating portion of the sunspot. The straight line SL refers to the vertical slice to examine the current distribution across the sigmoid structure. Second column: side view of the field structure in the corresponding panels of the first column. It indicates the flux rope structure with twisted core and overlying potential field envelope. Third column: current distribution $|\mathbf{J}|$ (mAm^{-2}) in the vertical slice SL shown in the last panel of the first column. White curves are contours of B_z obtained in the same SL. Note the strong current concentrations located low in the height overlaid by weak current concentrations of the less sheared arcade.

3.4. Eruption Event of 2014 September 8

A moderate eruption occurred in this AR at 23:50UT when the AR was at disc location of E30N15. It generated a major disturbance in the corona as a CME and M4.6 flare. Figure 6 illustrates the dynamical scenario of this eruption event from high-cadence multichannel AIA observations. For a simultaneous view, two combinations of composites are considered in this study. Composites prepared by AIA 94/335/193 channels (middle row panels) clearly present a well-developed structure of the sigmoid just before the main eruption. On the other hand, the composites prepared by AIA 131/171/304 Å (top row panels) show a rising continuous flux thread (as a main body of the flux rope) in the middle of the sigmoid channel. This is also clear from difference images of 131 Å where the very hot flux rope channel is essentially captured (bottom row panels). This is consistent with the recently settled debate on the time-instance of formation and appearance of the flux rope (Zhang et al. 2012; Cheng et al. 2013; Vemareddy & Zhang 2014) in the solar source regions. Here, the sigmoid structure (regarded as flux rope) preformed preferentially by the continuous action of sunspot rotation, and we see its existence as a continuous flux bundle

(embedded in a sheared arcade) only during initiation (around 23:00UT, top row panels) of its slow rise motion in the hot channels.

Since the flux rope has magnetic connections with the rotating part of the sunspot, a kink-instability is likely to be involved in the onset of the flux rope eruption by constantly injecting twist into the flux system constituting the main body of the sigmoid. This can be checked by relating α_{av} to twist number in the coronal loop constituting the sigmoid (Leamon et al. 2003). The total twist T of the coronal magnetic loop, assuming it to be a semicircle of length l with its footpoint separation distance d, is given by

$$T = lq = \frac{\pi d}{2}\frac{\alpha_{av}}{2} = l\frac{\alpha_{av}}{2}. \qquad (5)$$

Here, the winding rate is assumed to be half the value of α_{av} because it is not a well-known parameter. Since the local values of $\alpha = \frac{J_c}{B_z}$ are of order 10^{-6} m^{-1}, averaging over a small area at the flux rope leg in the sunspot region gives $>0.7 \times 10^{-7}$ m^{-1}. As the traced sigmoid length is about 190 Mm, the above expression implies a total twist of more than one turn (6.65
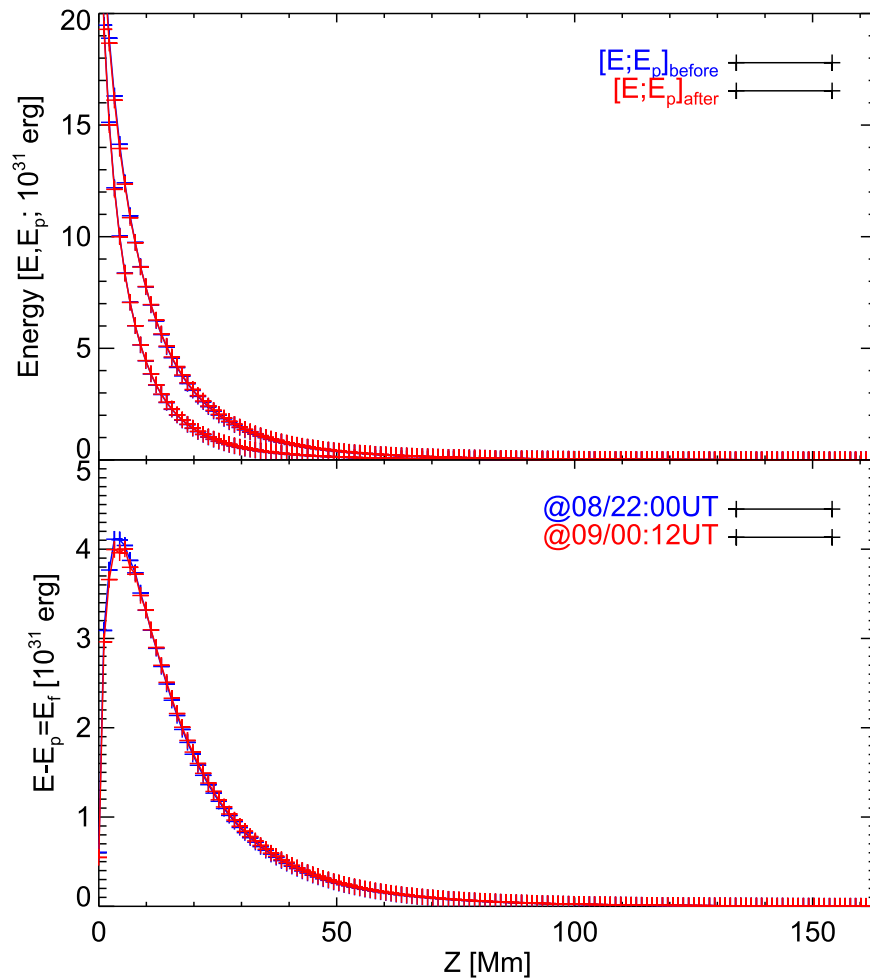
Figure 8. Evolution of magnetic energy before and after the eruption event of 2014 September 8 in the AR12158. Top: non-potential energy density and potential energy density are integrated over each horizontal plane and plotted as a function of height. Bottom: horizontally integrated free energy, as a function of height, before and after the eruption.

radians = 1.05 turns, note a 2π factor with turns). Note that high-resolution and high-cadence observations may improve the calculations in which case the α value, on average, may indicate the kink-nature of the field lines constituting the flux rope. Reconnection with the overlying field lines (Antiochos et al. 1999) in a later phase triggers the eventual eruption of this FR at 23:50UT, which follows the commencement of the M4.6 flare. Unlike the usual cases, the progressive reconnection during the post-flare phase lasts for 10 hr. Even after this long-duration flare event, the precursor sigmoid structure retains its geometry, indicating the eruption to be partial (Gilbert et al. 2007). The associated CME was captured in the LASCO/C3 field of view and found to have a linear speed of 230 km s^{-1}.[3]

Visualization of the field lines from the rotating portion in the sunspot suggests the development of the flux rope structure. In Figure 7, we plot those field lines for the snapshots around this eruption event. The lower field lines are progressively sheared by the sunspot rotation and become the twisted core of the overlying less sheared field lines. We then compute the current density in a vertical cross-section plane (slice SL) of

this flux rope structure and plot it in the corresponding panels of the third column. The distribution of B_z in the same-slice planes is also computed and its contours (± 500 G) over-plottedto identify the main polarities. Owing to stressed field lines all along the polarity inversion line of the sunspot and the negative polarity, the current distribution appears exactly as an arc shape and strong current concentration is co-spatial with the polarity inversion line. With the development of the twisted core structure, the current concentration above the negative polarity is enhanced (22:00UT panel). This is obvious even from the time profile of the net vertical current (Figure 3), where the surface integral of vertical current density increases rapidly (over a span of 5 hr) during this eruption event. We emphasize the difficulty of capturing the twisted or helical structures at the sigmoid sites due to lack of sufficient instrumental sensitivity for the horizontal polarization signal (Hoeksema et al. 2014) and the model of boundary-dependent extrapolation. This issue deserves a separate study with a different treatment of data-driven simulation (e.g., Wu et al. 2006; Jiang et al. 2014) and will be our future investigation.

It is a matter of interest to estimate the total magnetic energy $\left(E = \int_V \frac{B^2}{8\pi} dV\right)$ of the AR magnetic system under these evolving conditions. In addition to global energy content, we
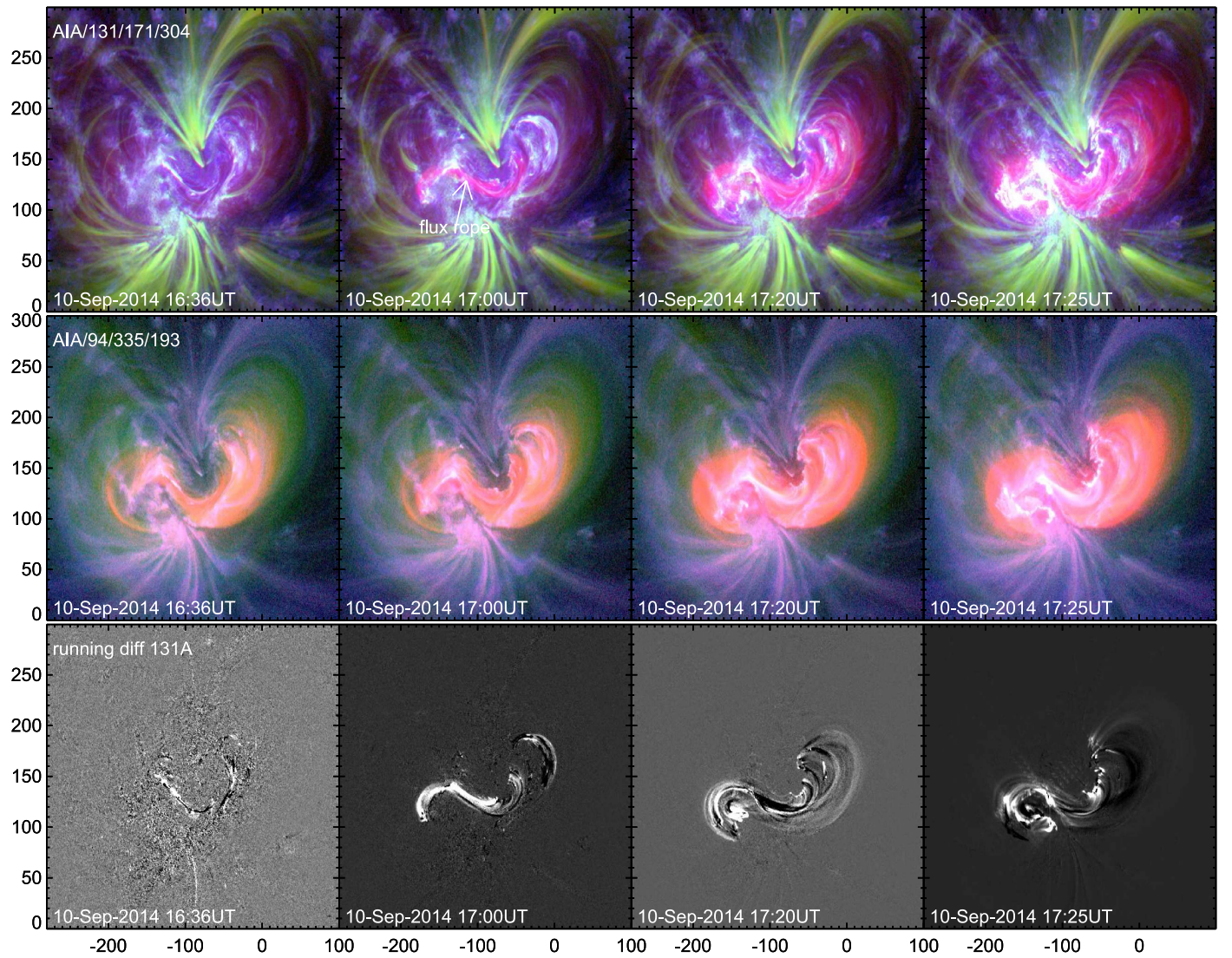
Figure 9. Same as Figure 6 but for the onset of sigmoid eruption of 17:30UT 2014 September 10. This eruption leads to an Earth-directed fast CME.

can also study the height variation of the magnetic free energy. For this, we compute the surface integral of the magnetic energy

$$E(z) = \int_S \frac{B^2}{8\pi} dx \, dy \qquad (6)$$

which gives the height-dependent energy content (e.g., Mackay et al. 2011). Using this expression, we compute potential field energy (E_p), total non-potential energy (E), and free magnetic energy ($E_{\mathrm{free}} = E - E_p$) before and after the enhancement of the total current (i.e., eruption event) in the AR magnetic structure. They are plotted in Figure 8 with respect to height from the photosphere into the corona. We can see from these height profiles that E and E_p are predominantly located below 20 Mm. Although they minutely differ from one another, the E_f curves are well distinguished. E_f is mainly situated in the height range of 2–40 Mm with a maximum at about 6 Mm.

From these profiles, we can calculate the global energy loss/gain during this eruption. We found the free energy before (22:00UT on September 8) and after (00:12UT on September 9) as 79.8×10^{31} erg, 79.7×10^{31} erg respectively. The free magnetic energy that would be available for this event is

positive (0.1×10^{31} erg). Although this is marginally sufficient to power the observed flare, it is still small for an eruption. The reason lies in the fact that the observed field components showed increased net vertical current around this event; however, snapshots just before and after this event detect the available free energy. Moreover, the required energy for this M-class flare is released from a localized region by field reconfiguration and averaging over the entire volume may not detect it over a globally building scenario. Since the eruption is associated with a low speed CME, it is likely that the released energy is small.

3.5. Eruption Event of 2014 September 10

A second major eruption from AR 12158 occurred on 2014 September 10 at 17:25UT. Since the AR was at the disc location of E5N15, the CME eruption was face-on to the Earth and a halo CME at a linear speed of 1071 km s^{-1} registered in LASCO white-light CME observations. Unlike the earlier event, this is a full successful eruption distinguished by the speed of the CME and the nature of speed of reconnection associated with the flare, which is X1.6. In Figure 9, we display snapshots of the coronal imaging observations during the onset
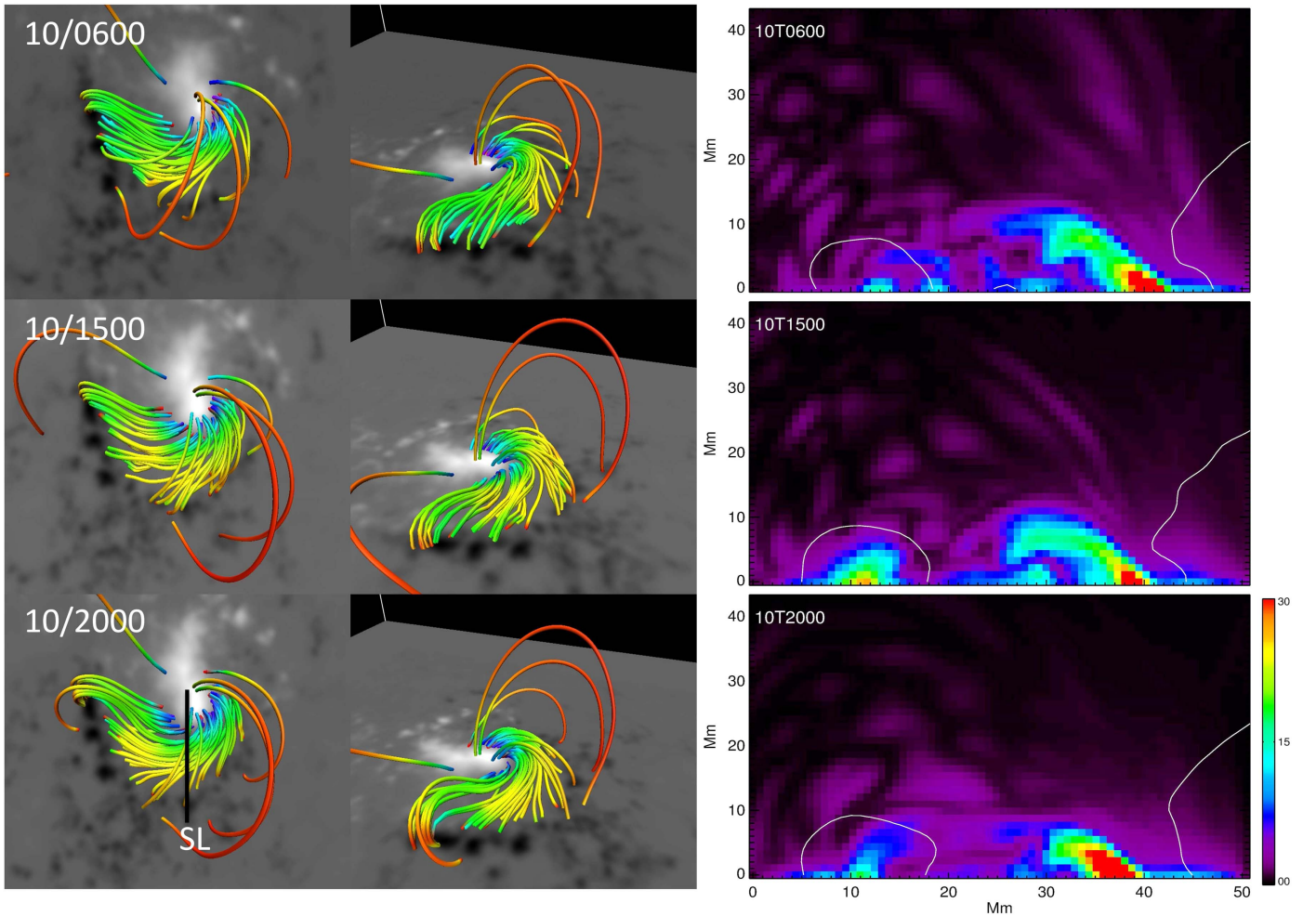
Figure 10. Same as Figure 7 but during the sigmoid eruption event of 17:30UT 2014 September 10. In all three slices, total current density smears away probably due to dissipation by reconnection.

of the eruption. The eruption commences from 16:45UT; since then the visibility of the continuous trace of the flux rope becomes apparent in the composite images of 131/171/304 Å. Increasingly enhanced emission all along the sigmoid is likely be a consequence of reconnection in a thinning current sheet that would form below the flux rope (Gibson et al. 2006, second row panels of 94/335/193 composites). Like the earlier event, this event is also suggested to be a consequence of helical kink instability triggered under the continuous slow driven motion by the sunspot rotation. The evidence comes from the analysis of the localized distribution of α as described for the previous event.

The field structure seen in the snapshots around this event also suggest a flux rope (Figure 10). The core part is not as strongly twisted as in the earlier case but overlaid by a sheared arcade. Strong current concentrations due to the sheared arcade system of the sigmoid are distributed up to a height of 15 Mm well before this eruption. These current concentrations are located along and above the PIL owing to the stressed field between the sunspot and its surrounding opposite polarity. Moreover, the appearance of the fluxrope in the EUV channels is only during the onset time, which is too highly dynamic to be followed by the static models based on observed static photospheric frames. Despite this known difficulty, the current distribution in the slice "SL" during the pre-to-post eruption

(from top to bottom) phase, we note the degrading current concentrations, reflecting the indications of the field transition from the non-potential sheared arcade to the potential field. For this reason, the energy estimations, as for the earlier event, also imply a similar outcome of lowering the free energy.

In the top panel of Figure 11, we plot the horizontally integrated total magnetic energy and potential energy as a function of height, before (06:00UT on 2014 September 10) and after (20:00UT on 2014 September 10) the eruption. Because the extrapolation problem is boundary dependent, the chosen times for this energy calculation are according to the time profile of the net vertical current (Figure 3, even α_{av}) where a drastic decrease of net vertical current in both polarity regions is observed. Consistent with the current distribution, the free-energy predominantly lies within 40 Mm, peaking at around 6 Mm. The free-energy curve after eruption is well below that before eruption since the field is relaxed and less non-potential. During this static field evolution at the background of the observed dynamic eruption, the energy release is estimated to be 1.05×10^{32} erg, which is sufficient to power a GOES class X1.6 magnitude flare.

4. SUMMARY AND DISCUSSION

In this work, we investigated the relation of sunspot rotation to the major eruptions occurring in its vicinity. Vortex-like
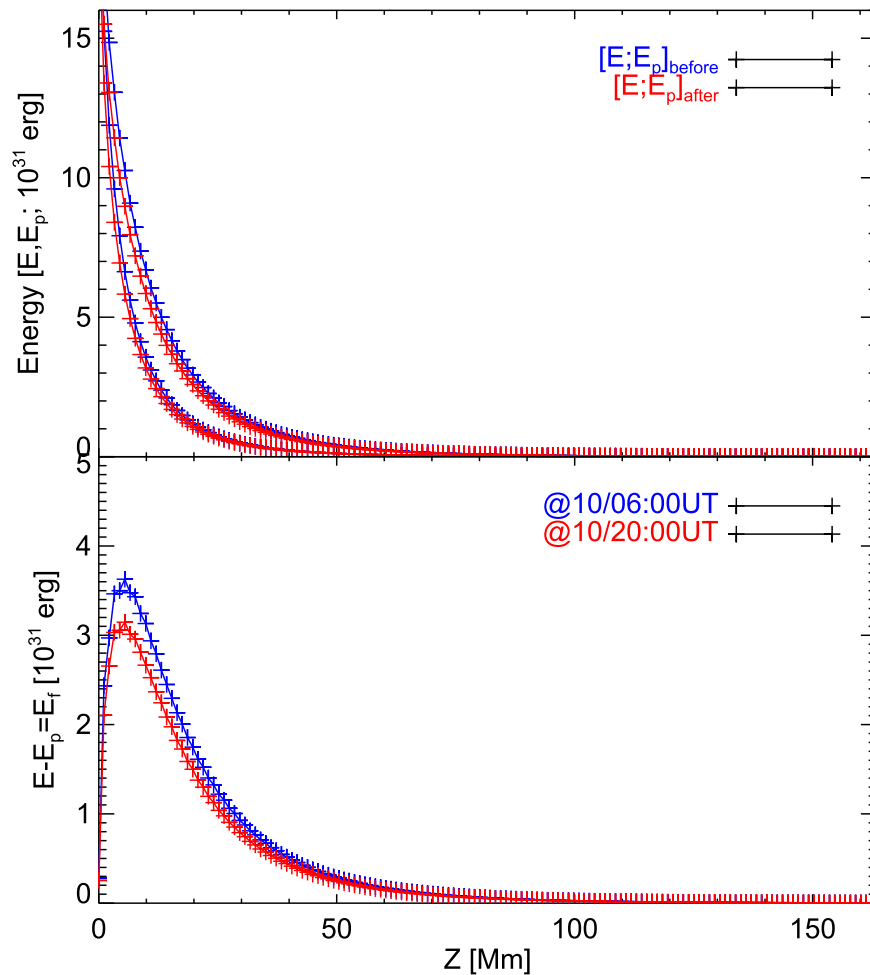
Figure 11. Same as Figure 8 but for the sigmoid eruption event of 17:30UT 2014 September 10 in the AR12158.

motions are modeled to be potential triggers of eruptions in the ARs (Amari et al. 1996; Török & Kliem 2003; Török et al. 2013) by progressively twisting the line-tied foot points. In particular, they are involved in the formation or development of twisted flux ropes and sigmoids by injecting twist and energy in the AR magnetic structure (e.g., Ruan et al. 2014). We found that the location of the sunspot rotation had the magnetic roots of the erupting sigmoid (associated to two CME eruptions) that existed along the PIL between the sunspot and the surrounding opposite polarity in the AR 12158 (Cheng et al. 2015). As in earlier reports (Vemareddy et al. 2012a), the correspondence of sunspot rotation motion is obviously reflected in the many non-potential parameters (Figure 3) during the evolution of the AR. Unlike the earlier cases, this AR is in the post-emergent phase with decreasing flux content, which reveals the direct role of observed sunspot rotation, a purely surface phenomenon of sub-photospheric origin, in the two major sigmoid eruptions.

Since the driven motion by sunspot rotation is slow (of the order of $1 \, km \, s^{-1}$), the evolution of the magnetic structure is said to be quasi-static and therefore the evolution is approximated by a time series of force-free equilibria (e.g., Sun et al. 2013; Vemareddy & Wiegelmann 2014). Under this scenario, utilizing HMI 12 minute cadence vector magnetic field observations, the AR magnetic structure is reconstructed by an NLFF model, which reproduces the global structure as

resembling the coronal EUV plasma structure. The modeled magnetic structure around the rotating sunspot appears as a fan-like sheared arcade, manifesting the observed sigmoid. Acknowledging the difficulty in working with noisy observations (Hoeksema et al. 2014), and also tracing the same structure in all time snapshots, the modeled field indicates signatures of accumulating strong coronal current concentrations and a building sigmoid at different times.

While the sunspot was observed to be rotating, a moderate CME eruption occurred at 23:00UT on 2014 September 8. During the onset of eruption, AIA multi-thermal observations conspicuously revealed a continuous trace of hot flux rope embedded in the middle of an ambient less hot sheared structure (Zhang et al. 2012; Vemareddy & Zhang 2014; Cheng et al. 2015). The eruption is a partial one, where flare reconnection takes place slowly and accordingly a low-speed CME associated with a long-duration M4.6 flare is observed. Consistent with the photospheric measurement of net vertical current during the pre-to-post eruption, an increased coronal current concentration is observed across the sigmoid due to twisting by sunspot rotation. From these observations, the estimated free energy during the eruption is small, which we believe to be an averaging effect because energy is released locally during field reconfiguration.

A second CME eruption launched at 17:30UT on 2014 September 10 in the AR. The CME is a halo heading toward

Earth at a high speed (1014 km s^{-1}) and follows an X1.6 flare. The appearance of a continuous flux rope is evident amid the sigmoid during the onset of the eruption. From the net vertical current during this eruption event, the coronal current concentrations degrade across the sigmoid and the free energy estimation indicates a release of 1.44×10^{31} erg, which is sufficient for an X-class flare. These analysis results suggest that the magnetic connections of the sigmoid are driven by the slow motion of the sunspot rotation, which developed to a highly twisted flux rope structure in a dynamical scenario. Exceeding the critical twist in the flux rope explains the loss of equilibrium, triggering the onset of the observed eruptions. Although the NLFFF extrapolation works best in reproducing the highly twisted structure around the sunspot, given the limitations of both the observations and the model, a realization of a clear flux rope structure, which is dynamic in nature, seems to be a difficult task. Data-driven MHD based models (e.g., Wu et al. 2006; Jiang et al. 2012a, 2014) would help to better explain the observed features in eruptions under the influence of sunspot rotation; this will be the subject of our future investigations.

REFERENCES

Amari, T., Aly, J.-J., Mikic, Z., & Linker, J. 2010, ApJL, 717, L26
Amari, T., Luciani, J. F., Aly, J. J., & Tagger, M. 1996, ApJL, 466, L39
Antiochos, S. K., DeVore, C. R., & Klimchuk, J. A. 1999, ApJ, 510, 485
Aulanier, G., Török, T., Démoulin, P., & DeLuca, E. E. 2010, ApJ, 708, 314
Barnes, C. W., & Sturrock, P. A. 1972, ApJ, 174, 659
Berger, M. A., & Field, G. B. 1984, JFM, 147, 133
Bhatnagar, A. 1967, KodOB, A180
Bobra, M. G., Sun, X., Hoeksema, J. T., et al. 2014, SoPh, 289, 3549
Brown, D. S., Nightingale, R. W., Alexander, D., et al. 2003, SoPh, 216, 79
Cheng, X., Ding, M. D., & Fang, C. 2015, ApJ, 804, 82
Cheng, X., Zhang, J., Ding, M. D., et al. 2013, ApJL, 769, L25
Evershed, J. 1910, MNRAS, 70, 217
Galsgaard, K., & Nordlund, Å. 1997, JGR, 102, 219
Gerrard, C. L., Arber, T. D., & Hood, A. W. 2002, A&A, 387, 687
Gibson, S. E., Fan, Y., Török, T., & Kliem, B. 2006, SSRv, 124, 131
Gilbert, H. R., Alexander, D., & Liu, R. 2007, SoPh, 245, 287
Hagino, M., & Sakurai, T. 2004, PASJ, 56, 831
Hiremath, K. M., & Suryanarayana, G. S. 2003, A&A, 411, L497
Hoeksema, J. T., Liu, Y., Hayashi, K., et al. 2014, SoPh, 289, 3483
Jiang, C., Feng, X., Wu, S. T., & Hu, Q. 2012a, ApJ, 759, 85
Jiang, C., Wu, S. T., Feng, X., & Hu, Q. 2014, ApJ, 780, 55
Jiang, Y., Zheng, R., Yang, J., et al. 2012b, ApJ, 744, 50
Kazachenko, M. D., Canfield, R. C., Longcope, D. W., et al. 2009, ApJ, 704, 1146
Kusano, K., Maeshiro, T., Yokoyama, T., & Sakurai, T. 2002, ApJ, 577, 501
Leamon, R. J., Canfield, R. C., Blehm, Z., & Pevtsov, A. A. 2003, ApJL, 596, L255
Lemen, J. R., Title, A. M., Akin, D. J., et al. 2012, SoPh, 275, 17
Liu, Y., & Schuck, P. W. 2012, ApJ, 761, 105
Mackay, D. H., Green, L. M., & van Ballegooijen, A. 2011, ApJ, 729, 97
McIntosh, P. S. 1981, in The Physics of Sunspots, ed. L. E. Cram & J. H. Thomas (Sunspot, NM: Sacramento Peak Observatory), 7
Mikic, Z., Schnack, D. D., & van Hoven, G. 1990, ApJ, 361, 690
Nindos, A., Patsourakos, S., & Wiegelmann, T. 2012, ApJL, 748, L6
Ruan, G., Chen, Y., Wang, S., et al. 2014, ApJ, 784, 165
Savcheva, A., & van Ballegooijen, A. 2009, ApJ, 703, 1766
Schou, J., Scherrer, P. H., Bush, R. I., et al. 2012, SoPh, 275, 229
Schuck, P. W. 2008, ApJ, 683, 1134
Stenflo, J. O. 1969, SoPh, 8, 115
Sun, X., Hoeksema, J. T., Liu, Y., et al. 2012, ApJ, 748, 77
Sun, X., Hoeksema, J. T., Liu, Y., et al. 2013, ApJ, 778, 139
Suryanarayana, G. S. 2010, NewA, 15, 313
Tian, L., & Alexander, D. 2006, SoPh, 233, 29
Tian, L., Alexander, D., & Nightingale, R. 2008, ApJ, 684, 747
Titov, V. S., Hornig, G., & Démoulin, P. 2002, JGRA, 107, 1164
Tokman, M., & Bellan, P. M. 2002, ApJ, 567, 1202
Török, T., & Kliem, B. 2003, A&A, 406, 1043
Török, T., & Kliem, B. 2005, ApJL, 630, L97
Török, T., Temmer, M., Valori, G., et al. 2013, SoPh, 286, 453
Vemareddy, P. 2015, ApJ, 806, 245
Vemareddy, P., Ambastha, A., & Maurya, R. A. 2012a, ApJ, 761, 60
Vemareddy, P., Maurya, R. A., & Ambastha, A. 2012b, SoPh, 277, 337
Vemareddy, P., Venkatakrishnan, P., & Karthikreddy, S. 2015, RAA, 15, 1547
Vemareddy, P., & Wiegelmann, T. 2014, ApJ, 792, 40
Vemareddy, P., & Zhang, J. 2014, ApJ, 797, 80
Wiegelmann, T. 2004, SoPh, 219, 87
Wiegelmann, T., & Inhester, B. 2010, A&A, 516, A107
Wiegelmann, T., Inhester, B., & Sakurai, T. 2006, SoPh, 233, 215
Wu, S. T., Wang, A. H., Liu, Y., & Hoeksema, J. T. 2006, ApJ, 652, 800
Yan, X.-L., Qu, Z.-Q., & Kong, D.-F. 2008, MNRAS, 391, 1887
Zhang, J., Cheng, X., & Ding, M.-. D. 2012, NatCo, 3, 747
Zhang, J., Li, L., & Song, Q. 2007, ApJL, 662, L35
Zhang, Y., Liu, J., & Zhang, H. 2008, SoPh, 247, 39
Zhao, J., Gilchrist, S. A., Aulanier, G., et al. 2016, ApJ, 823, 62